Chemical Engineering Journal 433 (2022) 133599

Contents lists available at ScienceDirect

Chemical Engineering Journal

journal homepage: www.elsevier.com/locate/cej

Theoretical study of structure sensitivity on Au doped CeO_2 surfaces for formaldehyde oxidation: The effect of crystal planes and Au doping

Meizan Jing [a,b,1], Weiyu Song [a,1], Yongfeng Li [c], Zhen Zhao [a,d], Jian Liu [a,*], Graeme Henkelman [b,*]

[a] State Key Laboratory of Heavy Oil Processing, College of Science, China University of Petroleum-Beijing, Beijing 102249, PR China
[b] Department of Chemistry and the Oden Institute for Computational Engineering and Sciences, University of Texas at Austin, Austin, TX 78712-0231, United States
[c] State Key Laboratory of Heavy Oil Processing, China University of Petroleum, Beijing 102249, PR China
[d] Institute of Catalysis for Energy and Environment, Shenyang Normal University, Shenyang 110034, PR China

ARTICLE INFO

Keywords:
HCHO removal
DFT
Au doped CeO_2 catalysts
Crystal plane effect
Oxygen vacancy

ABSTRACT

Engineering the surface structure of ceria-based catalysts at the atomic scale is a powerful strategy for boosting catalytic performance. Here, we carried out density functional theory calculations to investigate structure–activity relationships of Au-CeO_2 catalysts with (111), (110), and (100) surfaces exposed in common CeO_2 nanopolyhedra, nanorods and nanocubes, respectively. On stoichiometric $AuCe_{1-x}O_2$(111), (110) and (100) catalyst surfaces, HCHO oxidation follows the Mars van Krevelen mechanism. Calculations show that the migration of Au atoms on the surface of $AuCe_{1-x}O_2$(110) leads to a more stable configuration and improved HCHO oxidation performance than the undistorted (110) surface. On defective $AuCe_{1-x}O_2$(110) and (100) surfaces, HCHO oxidation follows the co-action of the Langmuir-Hinshelwood and Mars van Krevelen mechanisms with HCHO and O_2 co-participation and surface reduction by the removal of lattice oxygen. Adsorbed O_2 species contribute to a decrease in the energy barriers of the reaction steps. With the easy reducibility and lower energy barriers, the defect surfaces are more conducive to HCHO oxidation than stoichiometric surfaces. Whether stoichiometric surfaces or defective surfaces, (110) is most active for HCHO oxidation with the lowest activation energy for the rate-determining step, followed by (111), and then (100). Microkinetic simulations offer additional support for this result. Dopant Au atoms activate surface oxygen, and decrease the formation energy of oxygen vacancies. Au also reduces the energy barriers of key reaction steps on $AuCe_{1-x}O_2$(111) (110) (100) surfaces as compared to the pristine ceria surfaces. These calculations provide insight into the interaction between Au and CeO_2 with different surface terminations and the effect of the CeO_2 crystal plane and their reactivity for HCHO catalytic oxidation.

1. Introduction

Formaldehyde (HCHO), which is primarily released from buildings, decorative materials, and household products, is one of the most abundant and toxic indoor volatile organic compounds (VOCs) [1–3]. Having a carcinogenic-mutagenic-teratogenic effect, HCHO has been classified as a carcinogen [4] that can cause serious health issues, such as headaches, eye irritation, and even cancer [5,6]. The ever-increasing demand for better human health and more rigorous environmental regulation have motivated considerable interest in eliminating HCHO [7,8]. Complete catalytic oxidation of HCHO to CO_2 and H_2O at low temperature, with eco-friendly and energy-saving, has been considered a promising method for HCHO removal [1,3,9,10]. Noble metals (such as Pt, Pd, Au and Ag) supported on transition metal-oxide catalysts have attracted much attention for HCHO oxidation due to their high catalytic activities, good thermal stabilities, and synergetic strong metal-support interactions. Even though they have a lower catalytic activity for HCHO decomposition than supported Pt catalysts [1], an enormous effort has been made to study and improve the catalytic performance of Au-based catalyst by various preparation methods and supports [11–16].

Due to the unique redox properties associated with facile conversion between Ce^{3+} and Ce^{4+} states and its high oxygen storage capacity,

* Corresponding authors.
E-mail addresses: liujian@cup.edu.cn (J. Liu), henkelman@utexas.edu (G. Henkelman).
[1] These authors contributed equally as the first author.

https://doi.org/10.1016/j.cej.2021.133599
Received 30 August 2021; Received in revised form 6 November 2021; Accepted 10 November 2021
Available online 17 November 2021

CeO_2 is the most widely investigated support for Au-based Catalysts [16–18]. Engineering the surface structure at the nanoscale, such as the crystal shape of CeO_2, has proven an effective strategy to influence the catalytic performance of ceria catalysts for various reactions [19–22]. Si et al [23] identified a strong crystal plane effect of CeO_2 on gold-ceria activity for the WGS reaction. Au-CeO_2 nanorods with (1 1 0) and (1 0 0) facets show much greater catalytic activity than nanocubes with (1 0 0) facets and nanopolyhedra with (1 1 1) and (1 0 0) facets. Meanwhile, several experiments have studied the effect of crystal planes for HCHO oxidation in order to improve the activity on Au-CeO_2 catalysts. Bu et al.[24] compared the catalytic performance of Au/CeO_2 with different surface termination and showed that Au/CeO_2 nanorods (consisting primarily of (1 1 0) and (1 0 0) planes) are highly stable and active for HCHO oxidation at room temperature, as compared to commercial CeO_2 which primarily expose the (1 1 1) facet. The strong interaction between Au and the CeO_2 nanorod promotes the creation of oxygen vacancies and Au^{3+} near the interface, which in turn promotes the formation and conversion of formate. Xu et al.[25] showed that ceria nanorods supporting Au nanoparticles have a high reactivity for HCHO oxidation because the interaction between Au and CeO_2 induces a high concentration of oxygen vacancies. The structural properties of catalysts can greatly influence the reactivity of HCHO oxidation. However, there still a lack of fundamental theoretical understanding of how the morphology of the CeO_2 structures influence and explain the intrinsic structure-performance relationship of Au-CeO_2 catalysts with different surface termination. Additionally, there is an open question as to the role of Au and oxygen vacancies for HCHO oxidation. A comprehensive understanding of the structure-performance relationship of Au-CeO_2 catalysts should help guide and improve HCHO oxidation catalytic properties.

Herein, we present a mechanistic DFT study and microkinetic model of Au-CeO_2 catalysts with different crystal planes to explore structure-performance relationships for formaldehyde oxidation. To account for the particular morphology of nanoshapes, we choose the three lowest index and energy surfaces (1 1 1), (1 1 0), and (1 0 0), as these are the most exposed facets in three common structures: nanopolyhedra, nanorods and nanocubes, respectively [26]. In Au-CeO_2 catalysts, CeO_2 supported Au nanoparticles catalysts are fairly common in experimental research [15,16,25]. However, the type of Au doped CeO_2, as a form represented the strong interaction between gold and ceria, might also exist in experiments [16,27]. This is confirmed by the large adsorption energy of Au on Ce vacancy, suggesting a strong preference for Au atoms to enter into the ceria lattice [28]. Camellone also reported that Au substituted for Ce in lattice sites was more active than single Au^{+} species supported on CeO_2 surface for CO oxidation. Given the similarity between CO oxidation and HCHO oxidation, we consider Au doped CeO_2. The surface model for Au doped CeO_2 was constructed by replacing one of the surface Ce atoms by an Au atom, denoted as $AuCe_{1-x}O_2$. The oxygen vacancy model was simulated by removing a surface oxygen atom, denoted as $AuCe_{1-x}O_{2-y}$. This paper focuses on the structure sensitivity of HCHO oxidation on Au doped CeO_2(1 1 0) and (1 0 0) surfaces and a comparison with the Au doped CeO_2(1 1 1) surfaces that have been studied in our previous work [29]. Discussions of the effects of Au and oxygen vacancies on HCHO oxidation reaction are also included.

2. Computational details

2.1. DFT calculations

The DFT calculations were performed with the Vienna ab initio simulation package code [30,31]. The generalized gradient approximation with the PBE functional [32] was used to describe the electronic exchange–correlation energy. The projector augmented wave method [33,34] was used to describe the core-valence electron interactions; valence electrons were described with a plane wave basis set with a cutoff energy of 400 eV. The convergence criteria for the energy calculation and structure optimization were set to 1.0×10^{-4} eV and 0.05 eV/Å, respectively [29]. The Brillouin-zone integration [35] was sampled at the gamma point. A Gaussian smearing with a width of 0.05 eV was used to improve the convergence of states near the Fermi level. More stringent convergence criteria have been tested and the results show no significantly differences in energies [29,36,37]. The calculations included on-site Coulomb interactions (DFT + U) to describe the strong correlation effect among the partially filled Ce 4f states with a value of $U_{eff} = 4.5$ eV. The value of U_{eff} follows the approach described by Fabris et al., [38] Cococcioni and De Gironcoli [39].

Three common CeO_2 surface terminations of (1 1 1), (1 1 0), and (1 0 0) were chosen for the study. The CeO_2(1 1 1) surface consisted of a p (3×3) nine-atomic-layer supercell with the bottom three layers fixed. Additional details are provided in a previous study [29]. As shown in Fig. 1, the CeO_2(1 1 0) surface was modeled by a p(2×3) five-atomic-layer supercell with the bottom two layers fixed, and the CeO_2(1 0 0) surface was modeled by an O-terminated p(3×3) seven-atomic-layer supercell with the bottom two layers fixed [40]. To maintain the stoichiometry of the CeO_2(1 0 0) surface and reduce any dipole moment normal to the surface, a half oxygen monolayer was transferred from the surface to the bottom of the slab [26,41,42]. A set of test calculations based on a larger unit cell demonstrated the accuracy of these models (Figure S1-S2 and Table S1-S2 in Supplementary data). A vacuum layer of 15 Å was used to avoid interactions between periodic slab surfaces. The adsorption energy was calculated as,

E_{ads}= *E(adsorbate/surface)* - *E(adsorbate)* - *E(surface)*

where *E(adsorbate/surface)*, *E(adsorbate)* and *E(surface)* are the energies of the surface interacting with the adsorbate, and the isolated adsorbate and the bare surface, respectively. Transition states (TS) were found with the climbing image nudged elastic band (CI-NEB) method [43,44]. Frequency analysis was used to confirm that the transition states have only one imaginary frequency. The energy barrier and reaction energy are defined as

E_{TS}= *E(TS)* - *E(IS)*

ΔE = *E(FS)* - *E(IS)*

where *E(IS)*, *E(TS)* and *E(FS)* are the energies of the initial, transition and final states, respectively. The oxygen vacancy formation energy was calculated as:

$E_{O_v} = E_{surface\text{-}O_v} + \frac{1}{2}E_{O_2} - E_{surface}$

where $E_{surface}$, $E_{surface\text{-}O_v}$, and E_{O_2} are the energies of the clean surface, the defective surface with an oxygen vacancy, and a gas-phase O_2 molecule. Charge analyses were carried out using Bader's method [45].

2.2. Microkinetic simulations

Microkinetic simulations were used to describe the activity of Au doped CeO_2 (1 1 0) and (1 0 0) catalysts for HCHO oxidation. For surface reactions, the rate constants for the forward and backward elementary reactions were expressed by the Eyring equation:

$$k = Ae^{-\frac{E_a}{k_b T}}$$

where k, k_b, T, and E_a are the reaction rate constant in s^{-1}, the Boltzmann constant, temperature in Kelvin, and the activation barrier, respectively. A is the prefactor, which was approximated as 10^{13} s^{-1} for all the elementary surface reactions due to negligible entropy changes for the adsorbed species.

For non-activated molecular adsorption, the rate of adsorption was determined by the rate of surface impingement of gas-phase molecules. The molecular adsorption rate constant was described by Hertz-Knudsen kinetics [46]:

$$k_{ads} = \frac{PA^{*}}{\sqrt{2\pi m k_b T}} S$$

where P is the partial pressure of the adsorbate in the gas phase, A^{*} is the surface area of adsorbed site, m is the mass of adsorbate and S is the

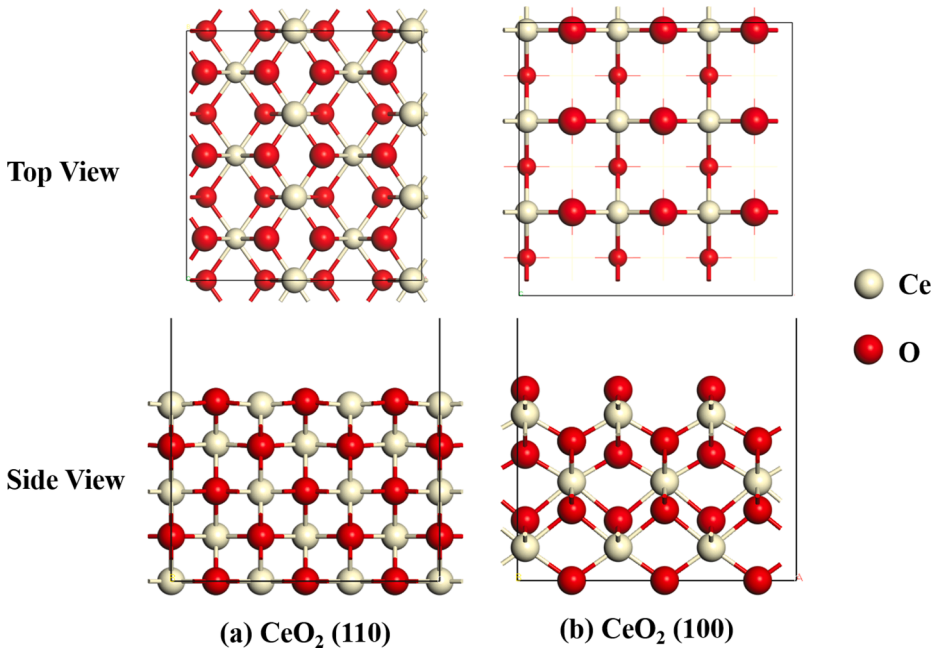

Fig. 1. Optimized structures of (a) CeO_2(1 1 0) and (b) CeO_2(1 0 0) (color scheme: light yellow-Ce; red-O; the same below).

sticking coefficient. For desorption, it is assumed that there are three rotational degrees of freedom and two translational degrees of freedom in the transition state. Accordingly, the rate of desorption is given by

$$k_{des} = \frac{k_b T^3}{h^3} \frac{A^{'}(2\pi k_b)}{\sigma\theta_{rot}} e^{-\frac{E_{des}}{k_b T}}$$

where σ and θ are the symmetry number and the characteristic temperature for rotation, respectively and h is Planck's constant. E_{des} is the desorption energy.

All microkinetic simulations were performed using the MKMCXX software [47]. Our approach to microkinetic simulations has been presented elsewhere [48–50]. Differential equations for all the surface reaction intermediates were constructed using the rate constants and the set of elementary reaction steps. For kinetic calculations, the reaction rate of any component M is required, which was solved using:

$$r_i = \sum_{j=1}^{N} \left(k_j v_i^j \prod_{k=1}^{M} c_k^{v_k^j} \right)$$

where k_j is the elementary reaction rate constant, v_i is the stoichiometric coefficient of component i in the elementary reaction, and c_k is the concentration of component k on the catalytic surface.

Steady-state coverages were calculated by integrating the ordinary differential equations in time until the changes in the surface coverages were small. The rates of the individual elementary reaction steps were obtained from the calculated steady-state surface coverages.

To qualitatively determine the influence of any single step i to the overall reaction, the degree of rate control, $X_{RC,\,i}$, has been defined as:

$$X_{RC,i} = \frac{k_i}{r}\left(\frac{\partial r}{\partial k_i}\right)_{k_{j\neq i}, K_i} = \left(\frac{\partial lnr}{\partial lnk_i}\right)_{k_{j\neq i}, K_i}$$

where k_i, K_i and r are the rate constants, the equilibrium constant for step i and the reaction rate, respectively. A larger $X_{RC,\,i}$ value means a greater influence of step i on the overall reaction; the sum of the $X_{RC,\,i}$ values is unity.

3. Results and discussion

3.1. Structures of Au doped CeO_2(1 1 0) and (1 0 0) surfaces.

The optimized configurations of the stoichiometric $AuCe_{1-x}O_2$(1 1 0) and (1 0 0) surfaces are shown in Fig. 2. By replacing one of the surface Ce atoms by a Au atom, the surface model of stoichiometric $AuCe_{1-x}O_2$(1 1 0) was constructed [51] (Fig. 2a). The Au atom coordinates to four surface O atoms with Au-O bond distances of 2.10 Å, forming a symmetric structure. The Bader charge of Au is calculated to be + 1.32 |e|, suggesting an oxidation state of + 3 [52,53]. No Ce^{4+} is reduced to Ce^{3+} and there are no changes of the magnetic moments of cerium. The doping of Au^{3+} brings about the transformation of O^{2-} to O^{-} (dispersed on the four surface oxygen atoms, on average, labeled with pink in Fig. 2a). However, this stoichiometric $AuCe_{1-x}O_2$(1 1 0) is not a stable surface; it spontaneously converts to a more stable structure with the Au atom migrating to the side of the surface oxygen atoms, leaving two doubly-coordinated oxygen atoms (O_{2c}), similar to a Mn or Pt doped CeO_2(1 1 0) catalysts [37,40]. This transformation requires a low activation energy of 0.53 eV and is exergonic by 0.72 eV (Fig. 2b and Figure S3). The Au atom coordinates with two surface O atoms and two subsurface O atoms with distances between 2.00 and 2.03 Å. Au shows a valence of + 3 with a Bader charge of + 1.00 |e|. The excess charge induces a O^{2-} transition to O^{-} (delocalized on the uncoordinated O_{2c}, labeled with pink in Fig. 2b). Again, there are no changes in the magnetic moments of cerium. Fig. 2c shows the structure of the $AuCe_{1-x}O_2$(1 0 0) surface, where the Au atom is substituted at a Ce site on the CeO_2(1 0 0) surface. On the $AuCe_{1-x}O_2$(1 0 0) surface, the Au dopant is surrounded by two surface oxygen atoms with Au-O bond lengths of 1.90 Å. It is found that the distortion of the $AuCe_{1-x}O_2$(1 0 0) surface is smaller than on $AuCe_{1-x}O_2$(1 1 0). The calculated Bader charge of Au is + 0.43 |e|, indicating a formal valence of + 1. Magnetic moments show that no Ce^{3+} ion forms after Au doping. The electronic changes due to the Au dopant brings about the transformation of O^{2-} to O^{-} (delocalized on the two surface oxygens bonded to Au, labeled with pink in Fig. 2c, and the oxygen atoms at the bottom). Low-valence dopant Au disrupts the chemical bonds in the surface of the doped oxide and activates the oxygen atoms [54,55].

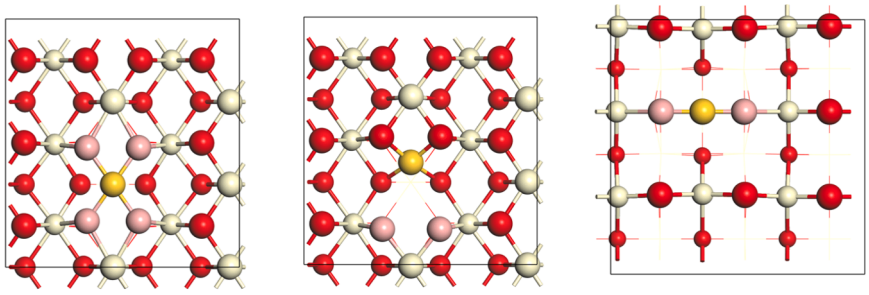

Fig. 2. Configurations of stoichiometric (a) $AuCe_{1-x}O_2$(1 1 0)-undistorted, (b) $AuCe_{1-x}O_2$(1 1 0)-distorted and (c) $AuCe_{1-x}O_2$(1 0 0) surfaces (color scheme: yellow-Au; pink-O^-; the same below).

3.2. Formations of oxygen vacancy on Au doped CeO_2 surfaces.

Owing to the facile Ce^{4+}/Ce^{3+} redox properties of ceria, large numbers of oxygen vacancies exist on the surfaces of ceria. By removing an oxygen atom, the $AuCe_{1-x}O_2$ surface is reduced to form an oxygen vacancy, as shown in the Fig. 3. Given the more stable structure and improved HCHO oxidation performance than the undistorted (1 1 0) surface (which will be discussed in section 3.3), we choose the $AuCe_{1-x}O_2$(1 1 0)-distorted surface to study oxygen vacancy formation. On the defective $AuCe_{1-x}O_{2-y}$(1 1 0) surface (Fig. 3a and 3b), the oxygen vacancy formation energy, formed by removing the O_{2c} and O_{3c} atoms, is −0.08 eV and 1.01 eV, respectively. The active O_{2c} species can be more easily removed than O_{3c}. On this surface, Au shows a + 3 valence charge (Bader charge of 1.11 $|e|$), and the excess electrons due to the oxygen vacancy leads to the formation of Ce^{3+} and O^{2-}. On the $AuCe_{1-x}O_2$(1 0 0) surface, when removing the surface O_{2c}, the Au atom spontaneously shifts position to bond with one surface and one subsurface oxygen (shown in the Fig. 3c). The calculated oxygen vacancy formation energy is only 0.1 eV. Au also shows + 1 valence (Bader charge of 0.81 $|e|$), and the excess electrons due to the formation of oxygen vacancy lead to the reduction of one O^- to O^{2-}.

We summarized the energies of oxygen vacancy formation on different crystal planes of CeO_2 and $AuCe_{1-x}O_2$ in Fig. 4. On the CeO_2(1 1 1), (1 1 0), and (1 0 0) surfaces, the oxygen vacancy formation energies are 2.24, 1.43 and 1.69 eV, respectively. While these are high energies, adding a doping metal is an effective way to decrease the oxygen vacancy formation energy in ceria [56]. With the doping of Au, the oxygen vacancy formation energies of those surfaces dramatically decrease to lower values of 0.17, −0.08 and 0.10 eV on $AuCe_{1-x}O_2$(1 1 1), (1 1 0), and (1 0 0) surfaces, respectively. Doping with the low-valence Au creates a Lewis acid on the surface and therefore facilitates oxygen vacancy formation (Lewis base) by a strong acid-base interaction [55]. The surface of a doped oxide has more oxygen vacancies than the pure host [54]. As discussed in Section 3.1, the electronic changes due to the doping of low-valence Au activate the surface oxygen, bring about the transformation of surface O^{2-} to O^- and make it more reactive, which explains the facile formation of oxygen vacancies on Au doped ceria surfaces.

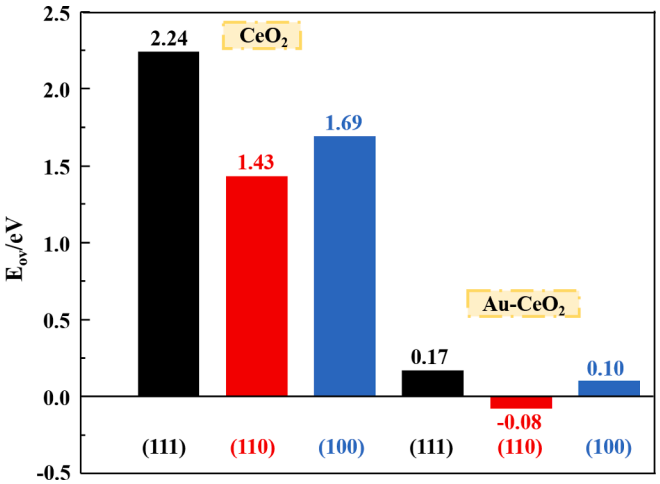

Fig. 4. The energies of oxygen vacancy formation on different crystal planes of CeO_2 and $AuCe_{1-x}O_2$.

It was established and predicted that the formation of oxygen vacancies on ceria is strongly surface sensitive [57,58]. As with the order of rods < cubes < polyhedra for the oxygen vacancy formation energy on CeO_2, Au doped CeO_2 follow the same sequence (Fig. 4). Among them, the $AuCe_{1-x}O_2$(1 1 0) possesses the property of facile oxygen vacancy formation with the lowest formation energy (-0.08 eV). The oxygen vacancies, which affect the catalytic activity of the catalysts (as discussed in section 3.3.4), are shown to be dependent on the shapes of the CeO_2 supports.

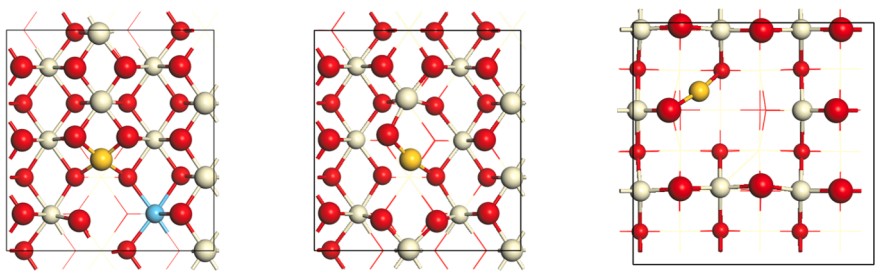

Fig. 3. Structures of defective (a)-(b) $AuCe_{1-x}O_{2-y}$(1 1 0) surfaces and (c) $AuCe_{1-x}O_{2-y}$(1 0 0) surface.

3.3. HCHO adsorption and oxidation reaction on the Au doped CeO_2 surfaces.

3.3.1. HCHO adsorption on the stoichiometric $AuCe_{1-x}O_2$ surface.

The optimized adsorption configurations of HCHO on the stoichiometric $AuCe_{1-x}O_2$(1 1 0) and (1 0 0) surfaces are shown in Fig. 5. On the $AuCe_{1-x}O_2$(1 1 0)-undistorted surfaces (Fig. 5a), HCHO adsorbs strongly at a bridge site with an exergonic energy of 1.75 eV. On the distorted surface (Fig. 5b), HCHO adsorbs with the C–H bond dissociating spontaneously and a stronger adsorption energy of −3.20 eV, as compared to the undistorted surface. The formaldehyde adsorption energies on CeO_2 and $AuCe_{1-x}O_2$ with different crystal planes are summarized in Table 1. The initial formaldehyde chemisorption values on the CeO_2(1 1 1), (1 1 0), and (1 0 0) surfaces are −0.88, −1.25, and −1.84 eV, respectively [26,59]. HCHO binds strongly on the $AuCe_{1-x}O_2$(1 1 1) and (1 1 0) surfaces, with adsorption energies of −1.17 and −3.20 eV, respectively. For the $AuCe_{1-x}O_2$(1 0 0) surface, the most stable adsorption geometry of HCHO is with the C connected with O_{2c} and the O bound to the surface Au. The calculated adsorption energy is −1.61 eV, weaker than HCHO adsorption on the CeO_2(1 0 0) surface.

3.3.2. HCHO oxidation reaction on the stoichiometric $AuCe_{1-x}O_2$ surfaces.

Fig. 6 shows the reaction pathway for the oxidation of HCHO to CO_2 and H_2O on the stoichiometric $AuCe_{1-x}O_2$(1 1 0)-distorted surface. Corresponding spin magnetic moment analysis of Ce and the Bader charge differences of Au are shown in Table S4. The reaction pathways on the stoichiometric $AuCe_{1-x}O_2$(1 1 0)-undistorted and $AuCe_{1-x}O_2$(1 0 0) surfaces are shown in the Supplementary data (S-3 and S-6).

The higher adsorption energy of HCHO than O_2 suggests that the stoichiometric $AuCe_{1-x}O_2$(1 1 0)-distorted surface should be preferentially occupied by HCHO instead of O_2 (Figure S7). Accompanied with HCHO adsorption, the C–H bond in the HCHO molecule spontaneously dissociates with the H atom adsorbing to the neighboring surface oxygen (Fig. 6, state ii, E_{ads} = -3.20 eV). The excess electrons due to C–H bond dissociation leads to the formation of Ce^{3+} and the reduction of O^- to O^{2-}. Next, the C–H cleavage of the adsorbed formate intermediate, the H from the C–H bond migrates to a surface O atom of ceria with the energy barrier and reaction energy of 0.50 and −1.65 eV, respectively (state TS1-iii). This C–H bond cleavage generates two excess electrons, which leads to the change of Au^{3+} to Au^+ (Bader charge of 0.58 $|e|$). Now, remaining on the surface are two OH groups and a CO_2 molecule. The desorption energy of CO_2 is found to be 0.09 eV, revealing that CO_2 can readily desorb to the gas phase at low temperature (state iv). With the removal of CO_2, an oxygen vacancy appears on the surface. Molecular oxygen adsorbs on this vacancy site strongly with an energy of −0.97 eV (state v). The O-O bond length is elongated to 1.42 Å (as compared to 1.21 Å in the gas phase), indicating the formation of a peroxide-type O_2^{2-} species. O_2 adsorption also causes the oxidation state of Au back to + 3. Then the O-O bond dissociates to form two oxygen atoms with a reaction energy of 0.49 eV and an activation barrier of 0.76 eV (state TS2-vi). One oxygen atom fills in the oxygen vacancy to be the lattice oxygen, and the other one is adsorbed on the surface Ce to be the adsorbed oxygen (state vi). Accompanied by O-O bond cleavage, the excess electron initially localized on the Ce atom returns to a surface oxygen atom. Next, the H atom of one adsorbed OH group dissociates so that the H relocates to the lattice oxygen (E_{TS} = 0.41 eV, ΔE = 0.29 eV, state TS3-vii). After that, the two H atoms migrate in succession to the adsorbed oxygen on the surface Ce to form an OH group (E_{TS} = 0.02 eV) and a H_2O molecule with the reaction energy of −0.50 and −0.51 eV, respectively (state TS4-ix). Finally, 0.75 eV is needed to desorb the H_2O molecule in order to complete the catalytic cycle. The potential energy diagram shows that the largest energy barrier is 0.76 eV corresponding to O-O bond cleavage (state TS2).

Table 1
The energies of HCHO adsorption on the CeO_2 and $AuCe_{1-x}O_2$ surfaces.

Catalysts	CeO_2 [26]			$AuCe_{1-x}O_2$		
	(1 1 1)	(1 1 0)	(1 0 0)	(1 1 1)	(1 1 0)	(1 0 0)
$E_{HCHO-ads}$/eV	−0.88	−1.25	−1.84	−1.17	−3.20	−1.61

For the two-step C–H bond cleavage mechanism, the energy barriers on the distorted surface are 0.0 and 0.50 eV, respectively, which are lower than those on the undistorted surface of 0.05 and 0.78 eV. The energy barrier of the rate-determining step also reduces as compared to the undistorted surface (0.95 eV for H_2O desorption) and the distorted surface (0.76 eV for O-O cleavage). The stronger HCHO adsorption, the lower energy barriers in the rate determining step and two-step C–H bond cleavage mean that the distortion of Au is beneficial to HCHO oxidation as compared to the undistorted surface. Thus, the following discussion of HCHO oxidation will be solely based on the $AuCe_{1-x}O_2$(1 1 0)-distorted surface.

On the stoichiometric $AuCe_{1-x}O_2$(1 1 1), (1 1 0), and (1 0 0) surfaces, HCHO oxidation follows the M−vK mechanism. We summarized the energy barriers in the key reaction steps on different surfaces of CeO_2, $AuCe_{1-x}O_2$ and $AuCe_{1-x}O_{2-y}$, as shown in Table 2, to elucidate the effect of Au doping and crystal planes. As listed in Table 2, Au doped in ceria facilitates a two-step C–H bond cleavage, one of which is the rate-determining step for HCHO oxidation in ceria [60], is significantly reduced. This is especially true of the (1 1 1) and (1 1 0) surfaces, where the energy barrier is lowered by half or more in comparison with the CeO_2(1 1 1) and (1 1 0) surfaces. On the stoichiometric $AuCe_{1-x}O_2$(1 1 1) and (1 1 0) surfaces, the rate-determining step for HCHO oxidation is the O-O bond cleavage with energy barriers of 0.94 and 0.76 eV, respectively. On the stoichiometric $AuCe_{1-x}O_2$(1 0 0) surface, the second C–H bond cleavage, with the largest energy barrier of 1.15 eV, becomes the rate determining step. Thus, the stoichiometric $AuCe_{1-x}O_2$(1 1 0) surface is the most active for HCHO oxidation, next is (1 1 1), followed by (1 0 0).

3.3.3. HCHO adsorption on the defective $AuCe_{1-x}O_{2-y}$ surfaces.

As discussed in Section 3.2, the low value of E_{ov} implies facile formation of oxygen vacancies on the $AuCe_{1-x}O_2$ surfaces. Thus, studying the formaldehyde adsorption and catalytic oxidation mechanism on the defective $AuCe_{1-x}O_{2-y}$ surfaces is significant.

On the defective $AuCe_{1-x}O_{2-y}$(1 1 0) and (1 0 0) surfaces (Fig. 7), after

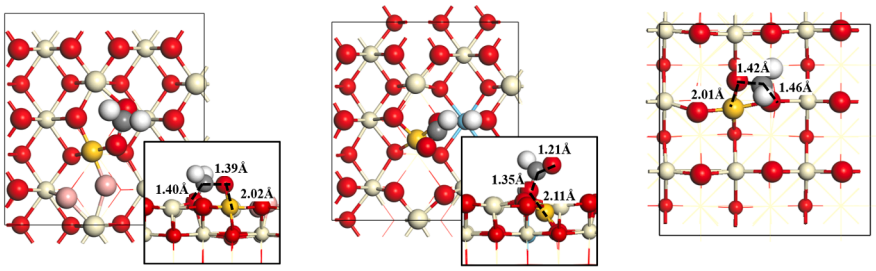

(a) $AuCe_{1-x}O_2$(110)-undistorted surface **(b) $AuCe_{1-x}O_2$(110)-distorted surface** **(c) $AuCe_{1-x}O_2$(100) surface**

Fig. 5. Adsorption configurations of HCHO on (a) $AuCe_{1-x}O_2$(1 1 0)-undistorted surface, (b) $AuCe_{1-x}O_2$(1 1 0)-distorted surface and (c) $AuCe_{1-x}O_2$(1 0 0) surface.

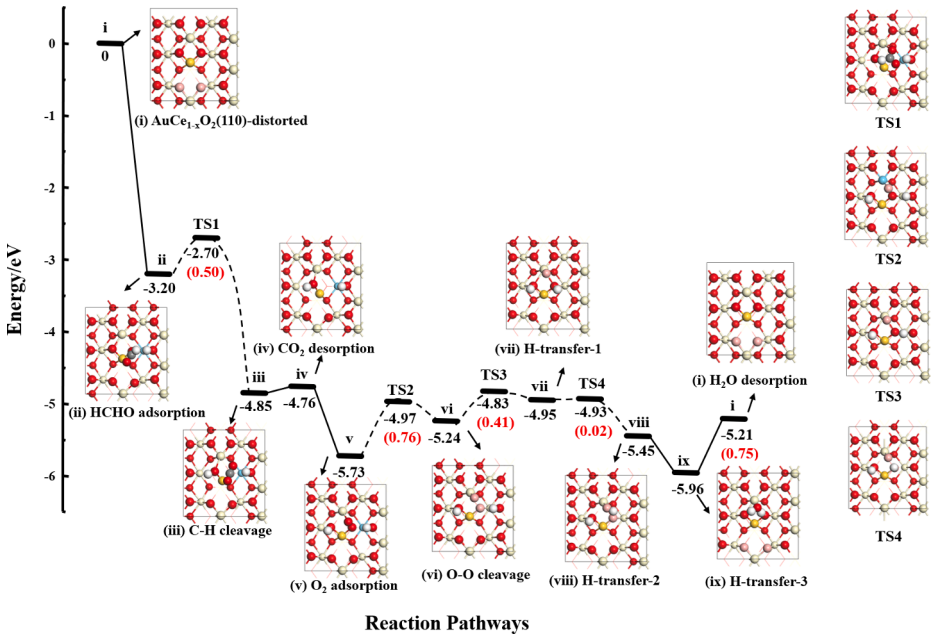

Fig. 6. HCHO oxidation reaction pathways on the stoichiometric $AuCe_{1-x}O_2$(1 1 0)-distorted surface.

Table 2
The energy barriers in some reaction steps on different surfaces of CeO_2, $AuCe_{1-x}O_2$ and $AuCe_{1-x}O_{2-y}$.

Catalysts	CeO_2 [26]			$AuCe_{1-x}O_2$			$AuCe_{1-x}O_{2-y}$		
	(1 1 1)	(1 1 0)	(1 0 0)	(1 1 1)	(1 1 0)	(1 0 0)	(1 1 1)	(1 1 0)	(1 0 0)
$E_{TS\ in\ 1\text{-}C\text{-}H\ cleavage}$ /eV	1.53	1.87	0.66	0.06	0.00	0.54	0.84	0.48	0.87
$E_{TS\ in\ 2\text{-}C\text{-}H\ cleavage}$ /eV	1.60	2.00	1.64	0.66	0.50	1.15	0.80	0.18	1.07
$E_{TS\ in\ O\text{-}O\ cleavage}$ /eV	–	–	–	0.94	0.76	0.29	0.80	0.46	0.02

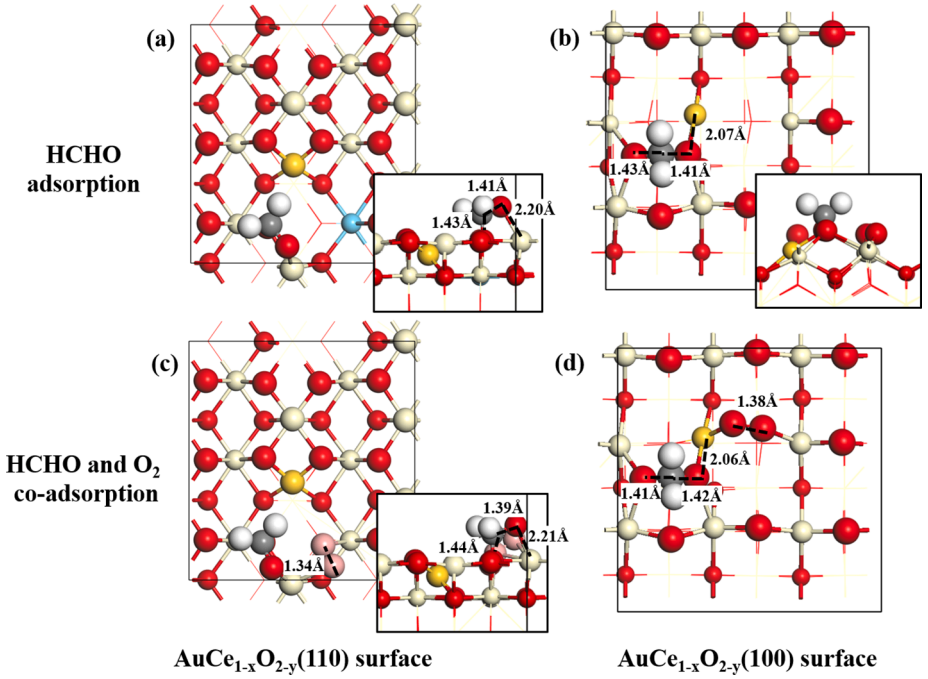

Fig. 7. (a)-(b) HCHO adsorption and (c)-(d) HCHO and O_2 co-adsorption configurations on the defective $AuCe_{1-x}O_{2-y}$(1 1 0) and (1 0 0) surfaces.

HCHO adsorbs to form dioxy-methylene with the O bonded to the Ce or the Au atom and the C bonded with surface oxygen (E_{ads} = -1.56 eV on (1 1 0), E_{ads} = -1.70 eV on (1 0 0)), molecular oxygen can fill the oxygen vacancy with an energy of −0.37 and −0.74 eV, respectively. Due to the separated active site for HCHO and O_2 adsorption, the co-adsorption configuration tends to form on the defective $AuCe_{1-x}O_{2-y}$(1 1 0) and

(1 0 0) surfaces. On the defective $AuCe_{1-x}O_{2-y}$(1 1 0) surface, Au also shows a + 3 valence (Bader charge of 0.97 |e|) with the adsorption of HCHO and O_2. The excess electron transfers from Ce^{3+} to the O_2 molecule, forming the superoxide O_2^- species with an O-O bond length of 1.34 Å. On the defective $AuCe_{1-x}O_{2-y}$(1 0 0) surface, the valence of Au changes from + 1 to + 3 with a Bader charge of 1.27 |e| after co-adsorption of HCHO and O_2. The excess electrons make the O-O bond elongate to 1.38 Å, which indicates the formation of a peroxide O_2^{2-} species.

3.3.4. HCHO oxidation reaction on the defective $AuCe_{1-x}O_{2-y}$ surfaces.

The cycle of elementary reaction steps for formaldehyde oxidation on the defective $AuCe_{1-x}O_{2-y}$(1 1 0)-distorted surface with O_2 participation is graphically represented in Fig. 8. The detailed spin magnetic moments of Ce and the Bader charge differences of Au in the different reaction stages are shown in Table S5. The reaction pathway on the defective $AuCe_{1-x}O_2$(1 0 0) surface is shown in the Supplementary data (S-7).

From the co-adsorbing state of HCHO and O_2 (Fig. 8, state iii), one of the C–H bonds of HCHO dissociates with the H migrating to the adsorbed O_2^- to generate an OOH species (state TS1-iv). The C–H cleavage is exergonic by 1.95 eV and the activation barrier is 0.48 eV. The two excess electrons generated in the C–H bond cleavage lead to the reduction of Ce^{4+} to Ce^{3+} and the formation of OOH^-. Then, the OOH species makes a breakage with the O atom being a lattice oxygen and the OH group transferring to a nearby Au atom (state v). Upon O-O bond cleavage, the excess electron transfers from Ce^{3+} to a surface oxygen. The reaction energy for OOH cleavage is endergonic by 0.46 eV. After the OOH cleavage and OH generation, the C–H bond from the formate group cleaves and protonates the OH group with an activation barrier of 0.18 eV and reaction energy of −0.89 eV (state TS2-vi). This step leads to the formation of CO_2 and H_2O and the generation of Au^+ with a Bader charge of 0.36 |e|. Upon desorption of H_2O (state vii, E_{des} = 0.28 eV) and CO_2 (state i, E_{des} = -1.18 eV), the surface is restored to the initial defective $AuCe_{1-x}O_{2-y}$(1 1 0)-distorted surface. The calculated energy barrier of the rate-determining step in the catalytic cycle is only 0.48 eV (1-C–H-cleavage, state TS1 and iv), suggesting high activity for HCHO oxidation at low temperature.

On the defective $AuCe_{1-x}O_{2-y}$(1 1 0) and (1 0 0) surfaces, accompanied with HCHO and O_2 co-adsorption and surface reduction by the removal of lattice oxygen, HCHO oxidation follows the co-action of the L-H and M−vK mechanisms. The exposed oxygen vacancies activate the oxygen molecule and contribute to the subsequent reaction steps. As shown in Table 2, compared with the energy barrier of 0.76 eV for the rate-determining step on the stoichiometric $AuCe_{1-x}O_2$(1 1 0) surface, the defective $AuCe_{1-x}O_{2-y}$(1 1 0) surface has a higher HCHO oxidation activity and a lower energy barrier of 0.48 eV. Therefore the adsorbed O_2^- species exhibits higher activity than lattice oxygen, which functions on the pristine $AuCe_{1-x}O_2$ surface. In comparison with the defective $AuCe_{1-x}O_2$(1 0 0) surface, with the activation energy of 1.07 eV, and the stoichiometric (1 0 0) surface with an activation energy of 1.15 eV, the adsorbed O_2^{2-} species also functions, just not as well as the O_2^- species. Due to the easily reducible surface and lower energy barriers, the defect surfaces are more conducive to HCHO oxidation. On the defective surfaces, (1 1 0) is also the most active for HCHO oxidation, next is (1 1 1), followed by (1 0 0).

3.3.5. Overview of the HCHO oxidation reaction on Au doped CeO_2 surfaces.

Here, the HCHO oxidation pathways on the stoichiometric and defective Au doped CeO_2(1 1 0), (1 0 0) surfaces are studied. Fig. 9(a) and (b) show the reaction scheme of the M−vK and co-action of the L-H and

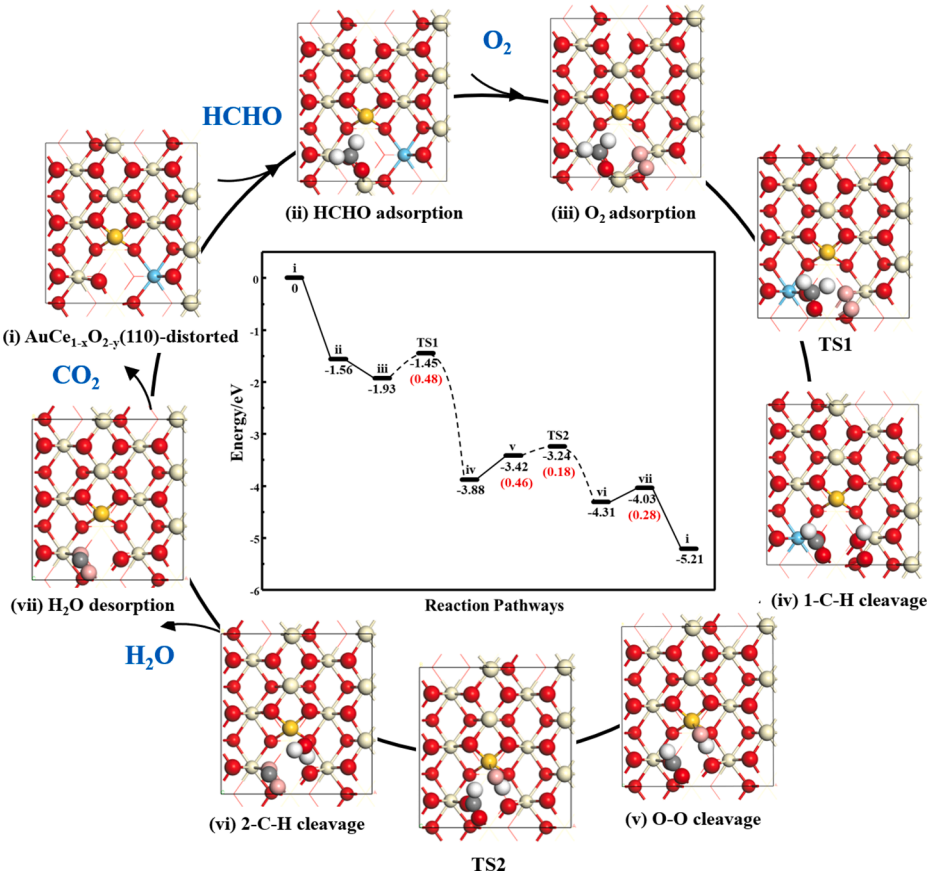

Fig. 8. HCHO oxidation reaction pathway on the defective $AuCe_{1-x}O_{2-y}$(1 1 0)-distorted surface.

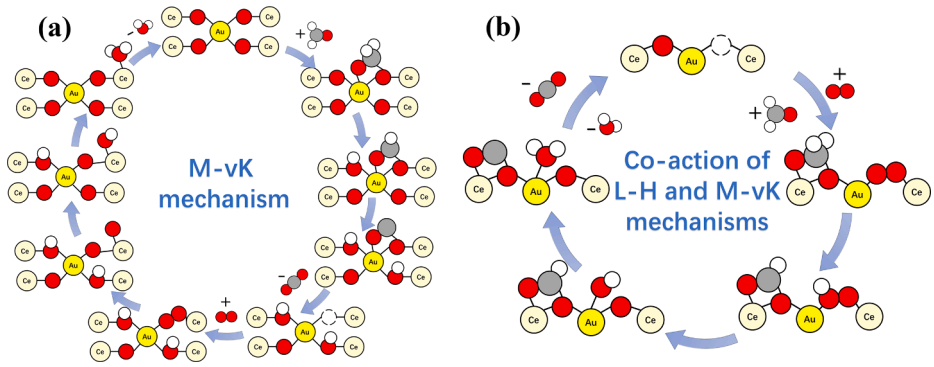

Fig. 9. The catalytic reaction pathway for HCHO oxidation on the (a) stoichiometric and (b) defective surfaces.

M−vK mechanisms for the formaldehyde oxidation reaction pathway on the stoichiometric and defective surfaces, respectively. On the stoichiometric surfaces, HCHO oxidation can be described as a M−vK type mechanism involving lattice oxygen atoms. First, HCHO adsorbs on the stoichiometric surface to form dioxy-methylene. Then, two C–H bonds cleave with the H atoms migrating to lattice O atoms to form OH and CO_2. Next, with CO_2 desorption, an oxygen vacancy is generated, upon which O_2 from the gas phase adsorbs and then dissociates. Next, the two dissociated H atoms transfer to a surface O atom to form water. Finally, H_2O desorbs to close the catalytic cycle. On the defective surfaces, HCHO oxidation follows the co-action of the L-H and M−vK mechanisms. It involves the co-adsorption of HCHO and O_2 and surface reduction by the removal of lattice oxygen. Starting from the co-adsorbed state, one C–H bond cleaves with H atom relocating to adsorbed O_2 species to form OOH. Then, the O-O bond of OOH dissociates to form a lattice oxygen and an adsorbed OH species. Next, the C–H bond cleaves with the H atom bonding with the OH species to form H_2O and CO_2. The desorption of CO_2 results in the release of lattice oxygen and surface reduction. Finally, with the desorption of H_2O and CO_2, the catalyst regenerates and is restored to its initial state.

3.4. Microkinetic analysis of the overall catalytic cycle.

From the calculated energetics of the HCHO oxidation catalytic cycle on different Au doped CeO_2 surfaces, we conclude that the order of reactivity follows (1 0 0) < (1 1 1) [29] < (1 1 0). To further validate the activity of Au doped CeO_2 system, microkinetic simulations were performed using the MKMCXX software to calculate the overall reaction rate under the room conditions (300 K, 1 atm, close to experimental conditions). Considering the actual oxidation condition of HCHO [15,16,25], the feed gas is composed of 100 ppm HCHO balanced with the air (21 vol% O_2 and 79 vol% N_2). The variation of reaction rate with the reaction temperature and partial pressure of reactants are also examined.

HCHO oxidation on the stoichiometric $AuCe_{1-x}O_2$(1 1 0) and (1 0 0) surfaces follow the M−vK mechanism with participation of adsorbed HCHO and lattice oxygen. On the defective $AuCe_{1-x}O_{2-y}$(1 1 0) and (1 0 0) surfaces, the HCHO oxidation cycle can be described by the co-action of the L-H and M−vK mechanisms. The elementary reaction steps and microkinetic results of HCHO oxidation on Au doped CeO_2(1 1 0) and (1 0 0) catalysts are shown in Table S8-S12 and summarized in Table 3. We assume that dissociated H goes into the gas phase instead of taking up a surface O site [61], which is reasonable because H subsequently desorbs from the O site and the O sites are not involved in the remaining steps. By comparing the overall reaction rates of the catalysts under the room conditions (Table 3), we can confirm that the most active catalyst is the defective $AuCe_{1-x}O_{2-y}$(1 1 0) surface with the highest reaction rate ($r = 4.27 \times 10^{1}\ s^{-1}$). The apparent activation energies also reflect the activities of the catalysts; the defective $AuCe_{1-x}O_{2-y}$(1 1 0) catalyst has the lowest apparent activation energy 16.3 kJ/mol and exhibits the fastest reaction rate at 300 K. Next is the stoichiometric $AuCe_{1-x}O_2$(1 1 0) distorted surface, HCHO oxidation takes place with the reaction rate of $1.48 \times 10^{-2}\ s^{-1}$, many orders of magnitude higher than that on stoichiometric $AuCe_{1-x}O_2$(1 1 0) undistorted surface ($r = 1.70 \times 10^{-11}\ s^{-1}$). These results also indicate a higher activity of the distorted surface as compared to the undistorted surface. On the stoichiometric and defective Au doped CeO_2(1 0 0) surfaces, the processes exhibit rather low reaction rates under room conditions (6.84×10^{-10} and $8.21 \times 10^{-6}\ s^{-1}$, respectively), and thus (1 0 0) is the lowest-reactive plane. In comparison with the reaction rates on perfect and defective (1 1 0) (1.48×10^{-2} vs. $4.27 \times 10^{1}\ s^{-1}$), (1 0 0) ($6.84 \times 10^{-10}$ vs. $8.21 \times 10^{-6}\ s^{-1}$) surfaces, we can deduce that oxygen vacancy is beneficial to the overall HCHO oxidation catalytic activity.

The HCHO oxidation reaction rate as a function of temperature and pressure on $AuCe_{1-x}O_{2-y}$(1 1 0) surface is shown in Fig. 10a. It is obvious that the oxidation rate increases gradually when the pressure rises, but decreases over 1.8 atm. The reaction rate is greatly improved with an increase of temperature when below 375 K; however, over 375 K, it declines, and especially over 525 K. The best HCHO oxidation rate is at low temperatures because O_2 adsorption on an oxygen vacancy on $AuCe_{1-x}O_{2-y}$(1 1 0) surface is unfavorable at high temperature. The surface coverage of intermediates as a function of temperature (Fig. 10b) offers support for this view with the large coverage of HCHO*$AuCeO_{2x}$. At higher temperature (>525 K), the decrease of the adsorbed HCHO species and increase of *$AuCeO_{2x}$ lead to the drop of reaction rate.

4. Conclusion

DFT + U calculations of formaldehyde oxidation on different Au-CeO_2 surfaces have been performed to investigate the structure

Table 3
Forward (r_f), backward (r_b), and overall (r) reaction rates and rate-controlling step for HCHO oxidation reactions at Au doped CeO_2 catalysts.

Catalysts	Apparent activation energy/kJ.mol^{-1}	r_f/s^{-1}	r_b/s^{-1}	r/s^{-1}	Rate-controlling step
$AuCe_{1-x}O_2$ (1 1 0)-undistorted	176	1.70E-11	0.00E + 0	1.70E-11	H_2O*$AuCeO_2$ ↔ H_2O+*$AuCeO_2$
$AuCe_{1-x}O_2$ (1 1 0)-distorted	86.5	1.51E-2	3.09E-4	1.48E-2	H + O*O*$AuCeO_{2x}$ ↔ OH* O*$AuCeO_{2x}$
$AuCe_{1-x}O_{2-y}$ (1 1 0)	16.3	4.27E + 1	3.64E-29	4.27E + 1	O_2* HCHO*$AuCeO_{2x}$ ↔ O_2H*CHO*$AuCeO_{2x}$
$AuCe_{1-x}O_2$ (1 0 0)	164	6.84E-10	0.00E + 0	6.84E-10	H_2O*$AuCeO_2$ ↔ H_2O+*$AuCeO_2$
$AuCe_{1-x}O_{2-y}$ (1 0 0)	102	8.21E-6	1.17E-39	8.21E-6	O_2H*CHO*$AuCeO_{2x}$ ↔ O_2H*CO_2*$AuCeO_{2xx}$ + H

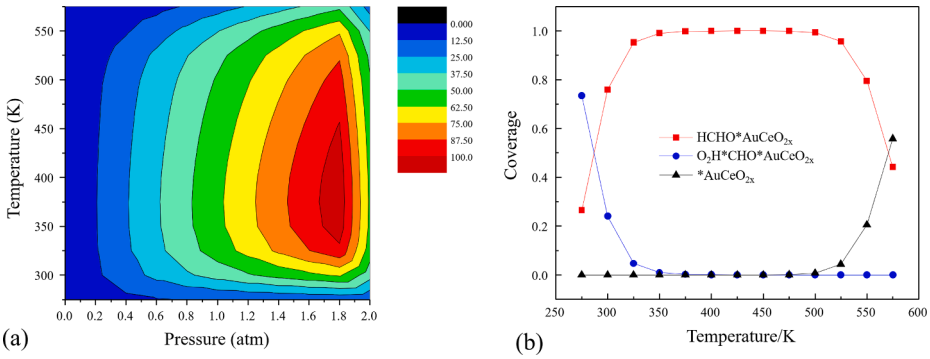

Fig. 10. The (a) overall reaction rate (s^{-1}) as a function of temperature and pressure (b) surface coverage of intermediate species as a function of temperature for HCHO oxidation on $AuCe_{1-x}O_{2-y}$(1 1 0)-distorted surface. Intermediates with a surface coverage near zero are not shown.

sensitivity and the role of Au doping and oxygen vacancies. On the stoichiometric $AuCe_{1-x}O_2$(1 1 0), (1 1 0), and (1 0 0) catalysts, HCHO oxidation follow the M−vK type mechanism involving adsorbed HCHO and surface oxygen. The reactions proceed via HCHO adsorption, C–H bond cleavages, CO_2 desorption, O_2 adsorption, H_2O formation and desorption. A doped Au atom on the $AuCe_{1-x}O_2$(1 1 1) and (1 0 0) surfaces is fairly stable as bound to adjacent oxygen atoms. A more stable $AuCe_{1-x}O_2$(1 1 0) structure forms with a small migration of the Au atom and shows improved HCHO adsorption and oxidation performance. The energy barriers of the rate-controlling step (0.76 eV on the undistorted surface vs. 0.95 eV on the distorted surface) and reaction rates (1.48×10^{-2} s^{-1} vs. 1.70×10^{-11} s^{-1}) support that. On the defective $AuCe_{1-x}O_2$(1 1 0) and (1 0 0) catalysts, the processes of HCHO oxidation follows the co-action of the L-H and M−vK mechanisms with HCHO and O_2 co-participation and surface reduction by the removal of lattice oxygen. Adsorbed O_2 species on oxygen vacancies are beneficial to the overall HCHO oxidation catalytic activity. With the easy reducibility and lower energy barriers, the defect surfaces are more conducive to HCHO oxidation than stoichiometric surfaces. Whether stoichiometric surfaces or defective surfaces, (1 1 0) is the most active for HCHO oxidation with the lowest activation energy for the rate-determining step, followed by (1 1 1), and then (1 0 0). The Au dopant activates surface oxygen and enhances the formation of oxygen vacancies on all Au doped ceria (1 1 1), (1 1 0) and (1 0 0) surfaces. In the order of rods < cubes < polyhedra on CeO_2, Au doped CeO_2 follow the same sequence for oxygen vacancy formation. Among them, the $AuCe_{1-x}O_2$(1 1 0) possesses facile oxygen vacancy formation with the lowest formation energy (-0.08 eV). Au also effects the HCHO oxidation reaction causing decreased energy barriers on $AuCe_{1-x}O_2$(1 1 1), (1 1 0), and (1 0 0) surfaces when compared with the corresponding ceria surfaces. Au doped CeO_2 (1 1 0) catalyst, with facile oxygen vacancy formation, strong HCHO adsorption and low activation energy, has an excellent performance for HCHO oxidation. Among them, the defective $AuCe_{1-x}O_{2-y}$(1 1 0) catalyst with the highest reaction rate ($r = 4.27 \times 10^{1}$ s^{-1}) and the lowest energy barrier (0.48 eV), exhibits a high activity for HCHO oxidation at room condition. Our microkinetic study of the HCHO catalytic oxidation cycle confirms our results that HCHO oxidation reaction to CO_2 and H_2O is highly sensitive to the exposed crystal planes, Au stability, and oxygen vacancy formation. These results shed light on the structure-performance relationship on Au-CeO_2 catalysts and demonstrate that engineering ceria structures is an effective strategy to boost HCHO oxidation activity.

Declaration of Competing Interest

The authors declare that they have no known competing financial interests or personal relationships that could have appeared to influence the work reported in this paper.

Acknowledgments

The authors are grateful for the financial support from National Natural Science Key Foundation of China (No. 22035009), the National Science Foundation of China University of Petroleum, Beijing (No. ZX20200079) and the State Key Laboratory of Heavy Oil Processing (No. 2021-03), and the China Scholarship Council (201806440115). The work at UT Austin was supported by the Welch Foundation (F-1841) and the Texas Advanced Computing Center.

Appendix A. Supplementary data

Supplementary data to this article can be found online at https://doi.org/10.1016/j.cej.2021.133599.

References

[1] L. Nie, J. Yu, M. Jaroniec, F.F. Tao, Room-temperature catalytic oxidation of formaldehyde on catalysts, Catal, Sci. Technol. 6 (11) (2016) 3649–3669, https://doi.org/10.1039/C6CY00062B.
[2] L. Miao, J. Wang, P. Zhang, Review on manganese dioxide for catalytic oxidation of airborne formaldehyde, Appl. Surf. Sci. 466 (2019) 441–453, https://doi.org/10.1016/j.apsusc.2018.10.031.
[3] C. He, J. Cheng, X. Zhang, M. Douthwaite, S. Pattisson, Z. Hao, Recent advances in the catalytic oxidation of volatile organic compounds: A review based on pollutant sorts and sources, Chem. Rev. 119 (7) (2019) 4471–4568, https://doi.org/10.1021/acs.chemrev.8b00408.
[4] International agency for cancer research (IACR) monographs on the evaluation of carcinogenic risks to humans, Formaldehyde, 2-Butoxyethanol and 1-tert-Butoxypropan-2-ol, WHO, Lyon France, 2006, 88.
[5] T. Salthammer, S. Mentese, R. Marutzky, Formaldehyde in the indoor environment, Chem. Rev. 110 (4) (2010) 2536–2572, https://doi.org/10.1021/cr800399g.
[6] M. Hakim, Y.Y. Broza, O. Barash, N. Peled, M. Phillips, A. Amann, H. Haick, Volatile organic compounds of lung cancer and possible biochemical pathways, Chem. Rev. 112 (11) (2012) 5949–5966, https://doi.org/10.1021/cr300174a.
[7] B. Bai, Q.i. Qiao, J. Li, J. Hao, Progress in research on catalysts for catalytic oxidation of formaldehyde, Chin. J. Catal. 37 (1) (2016) 102–122, https://doi.org/10.1016/S1872-2067(15)61007-5.
[8] A. Yusuf, C. Snape, J. He, H. Xu, C. Liu, M. Zhao, G.Z. Chen, B. Tang, C. Wang, J. Wang, S.N. Behera, Advances on transition metal oxides catalysts for formaldehyde oxidation: A review, Cat. Rev. 59 (3) (2017) 189–233, https://doi.org/10.1080/01614940.2017.1342476.
[9] H. Huang, Y. Xu, Q. Feng, D.Y.C. Leung, Low temperature catalytic oxidation of volatile organic compounds: a review, Catal, Sci. Technol. 5 (5) (2015) 2649–2669, https://doi.org/10.1039/C4CY01733A.
[10] J. QuirozTorres, S. Royer, J.-P. Bellat, J.-M. Giraudon, J.-F. Lamonier, Formaldehyde: Catalytic oxidation as a promising soft way of elimination, ChemSusChem 6 (4) (2013) 578–592, https://doi.org/10.1002/cssc.201200809.
[11] B. Chen, X. Zhu, M. Crocker, Y. Wang, C. Shi, Complete oxidation of formaldehyde at ambient temperature over γ-Al_2O_3 supported Au catalyst, Catal. Commun. 42 (2013) 93–97, https://doi.org/10.1016/j.catcom.2013.08.008.
[12] D.Y.C. Leung, X.L. Fu, D.Q. Ye, H.B. Huang, Effect of oxygen mobility in the lattice of Au/TiO_2 on formaldehyde oxidation, Kinet. Catal. 53 (2012) 239–246, https://doi.org/10.1134/S0023158412020048.
[13] C. Ma, D. Wang, W. Xue, B. Dou, H. Wang, Z. Hao, Investigation of formaldehyde oxidation over Co_3O_4-CeO_2 and Au/Co_3O_4-CeO_2 catalysts at room temperature: Effective removal and determination of reaction mechanism, Environ. Sci. Technol. 45 (2011) 3628–3634, https://doi.org/10.1021/es104146v.

[14] B. Chen, X. Zhu, M. Crocker, Y. Wang, C. Shi, FeO_x-supported gold catalysts for catalytic removal of formaldehyde at room temperature, Appl. Catal., B 154-155 (2014) 73-81. https://doi.org/10.1016/j.apcatb.2014.02.009.

[15] B. Chen, C. Shi, M. Crocker, Y. Wang, A. Zhu, Catalytic removal of formaldehyde at room temperature over supported gold catalysts, Appl. Catal., B 132-133 (2013) 245-255. https://doi.org/10.1016/j.apcatb.2012.11.028.

[16] H.-F. Li, N.a. Zhang, P. Chen, M.-F. Luo, J.-Q. Lu, High surface area Au/CeO_2 catalysts for low temperature formaldehyde oxidation, Appl. Catal., B 110 110 (2011) 279–285, https://doi.org/10.1016/j.apcatb.2011.09.013.

[17] B. Liu, C. Li, Y. Zhang, Y. Liu, W. Hu, Q. Wang, L. Han, J. Zhang, Investigation of catalytic mechanism of formaldehyde oxidation over three-dimensionally ordered macroporous Au/CeO_2 catalyst, Appl. Catal., B 111-112 (2012) 467-475. https://doi.org/10.1016/j.apcatb.2011.10.036.

[18] J. Zhang, Y. Jin, C. Li, Y. Shen, L. Han, Z. Hu, X. Di, Z. Liu, Creation of three-dimensionally ordered macroporous Au/CeO_2 catalysts with controlled pore sizes and their enhanced catalytic performance for formaldehyde oxidation, Appl. Catal., B 91 (2009) 11–20, https://doi.org/10.1016/j.apcatb.2009.05.001.

[19] A. Trovarelli, J. Llorca, Ceria catalysts at nanoscale: How do crystal shapes shape catalysis? ACS Catal. 7 (7) (2017) 4716–4735, https://doi.org/10.1021/acscatal.7b01246.

[20] C. Yang, X. Yu, S. Heißler, A. Nefedov, S. Colussi, J. Llorca, A. Trovarelli, Y. Wang, Christof. Wöll, Surface faceting and reconstruction of ceria nanoparticles, Angew. Chem. Int. Ed. 56 (2017) 375-379. https://doi.org/10.1002/anie.201609179.

[21] Yuan Cao, Li Zhao, Torsten Gutmann, Yeping Xu, Lin Dong, Gerd Buntkowsky, Fei Gao, Getting insights into the influence of crystal plane effect of shaped ceria on its catalytic performances, J. Phys. Chem. C 122 (35) (2018) 20402–20409, https://doi.org/10.1021/acs.jpcc.8b0613810.1021/acs.jpcc.8b06138.s001.

[22] Marçal Capdevila-Cortada, Gianvito Vilé, Detre Teschner, Javier Pérez-Ramírez, Núria López, Reactivity descriptors for ceria in catalysis, Appl. Catal., B 197 (2016) 299–312, https://doi.org/10.1016/j.apcatb.2016.02.035.

[23] Rui Si, Maria Flytzani-Stephanopoulos, Shape and crystal-plane effects of nanoscale ceria on the activity of $Au-CeO_2$ catalysts for the water-gas shift reaction, Angew. Chem. 120 (15) (2008) 2926–2929, https://doi.org/10.1002/(ISSN)1521-375710.1002/ange.v120:1510.1002/ange.200705828.

[24] Y. Bu, Y. Chen, G. Jiang, X. Hou, S. Li, Z. Zhang, Understanding of $Au-CeO_2$ interface and its role in catalytic oxidation of Formaldehyde, Appl. Catal., B 260 (2020), 118138, https://doi.org/10.1016/j.apcatb.2019.118138.

[25] Quanlong Xu, Wanying Lei, Xinyang Li, Xiaoying Qi, Jiaguo Yu, Gang Liu, Jinlong Wang, Pengyi Zhang, Efficient removal of formaldehyde by nanosized gold on well-defined CeO_2 nanorods at room temperature, Environ. Sci. Technol. 48 (16) (2014) 9702–9708, https://doi.org/10.1021/es5019477.

[26] M. Capdevila-Cortada, M. García-Melchor, N. López, Unraveling the structure sensitivity in methanol conversion on CeO_2: A DFT + U study, J. Catal. 327 (2015) 58–64, https://doi.org/10.1016/j.jcat.2015.04.016.

[27] Yuenian Shen, Xuzhuang Yang, Yizheng Wang, Yanbing Zhang, Huaiyong Zhu, Ling Gao, Meilin Jia, The states of gold species in CeO_2 supported gold catalyst for formaldehyde oxidation, Appl. Catal. B-Environ. 79 (2) (2008) 142–148, https://doi.org/10.1016/j.apcatb.2007.09.042.

[28] Matteo Farnesi Camellone, Stefano Fabris, Reaction mechanisms for the CO oxidation on Au/CeO_2 catalysts: activity of substitutional Au^{3+}/Au^{+} cations and deactivation of supported Au^{+} adatoms, J. Am. Chem. Soc. 131 (30) (2009) 10473–10483, https://doi.org/10.1021/ja902109k.

[29] Meizan Jing, Weiyu Song, Lulu Chen, Sicong Ma, Jianlin Deng, Huiling Zheng, Yongfeng Li, Jian Liu, Zhen Zhao, Density functional theory study of the formaldehyde catalytic oxidation mechanism on a Au-doped $CeO_2(111)$ surface, J. Phys. Chem. C 122 (1) (2018) 438–448, https://doi.org/10.1021/acs.jpcc.7b0927610.1021/acs.jpcc.7b09276.s001.

[30] G. Kresse, J. Furthmüller, Efficient iterative schemes for ab initio total-energy calculations using a plane-wave basis set, Phys. Rev. B 54 (16) (1996) 11169–11186, https://doi.org/10.1103/PhysRevB.54.11169.

[31] G. Kresse, J. Furthmuller, Efficiency of ab-initio total energy calculation for metals and semiconductors using a plane-wave basis set, Comp. Mater. Sci. 6 (1996) 15–50, https://doi.org/10.1016/0927-0256(96)00008-0.

[32] J.P. Perdew, K. Burke, M. Ernzerhof, Generalized gradient approximation made simple, Phys. Rev. Lett. 77 (1996) 3865, https://doi.org/10.1103/PhysRevLett.77.3865.

[33] P.E. Blöchl, Projector augmented-wave method, Phys. Rev. B 50 (1994) 17953-17979. https://doi.org/10.1103/PhysRevB.50.17953.

[34] G. Kresse, D. Joubert, From ultrasoft pseudopotentials to the projector augmented-wave method, Phys. Rev. B 59 (3) (1999) 1758–1775, https://doi.org/10.1103/PhysRevB.59.1758.

[35] Hendrik J. Monkhorst, James D. Pack, Special points for Brillouin-zone integrations, Phys. Rev. B 13 (12) (1976) 5188–5192, https://doi.org/10.1103/PhysRevB.13.5188.

[36] H. Wu, S. Ma, W. Song, E.J.M. Hensen, Density functional theory study of the mechanism of formaldehyde oxidation on Mn-doped ceria, J. Phys. Chem. C 120 (2016) 13071-13077. https://doi.org/10.1021/acs.jpcc.6b03218.

[37] L. Chen, W. Song, M. Jing, H. Zheng, J. Liu, Z. Zhao, Z. Li, Influence of surface termination on formaldehyde oxidation by Mn-doped ceria: A density function theory study, Mol. Catal. 448 (2018) 30–37, https://doi.org/10.1016/j.mcat.2018.01.017.

[38] S. Fabris, S. de Gironcoli, S. Baroni, G. Vicario, G. Balducci, Reply to "Comment on 'Taming multiple valency with density functionals: A case study of defective ceria'", Phys. Rev. B 72 (2005), 237102 https://doi.org/10.1103/PhysRevB.72.237102.

[39] M. Cococcioni, S. de Gironcoli, Linear response approach to the calculation of the effective interaction parameters in the LDA+U method, Phys. Rev. B 71 (2005), 035105, https://doi.org/10.1103/PhysRevB.71.035105.

[40] Yan Tang, Yang-Gang Wang, Jun Li, Theoretical Investigations of $Pt_1@CeO_2$ Single-Atom Catalyst for CO Oxidation, J. Phys. Chem. C 121 (21) (2017) 11281–11289, https://doi.org/10.1021/acs.jpcc.7b00313.

[41] B. He, J. Wang, D. Ma, Z. Tian, L. Jiang, Y. Xu, S. Cheng, Interaction of Pd single atoms with different CeO_2 crystal planes: A first-principles study, Appl. Surf. Sci. 433 (2018) 1036–1048, https://doi.org/10.1016/j.apsusc.2017.10.134.

[42] Spezzati, G. A.D. Benavidez, A.T. DeLaRiva, Su, Y. J.P. Hofmann, S. Asahina, E.J. Olivier, J.H. Neethling, J.T. Miller, A.K. Datye, E.J.M. Hensen, CO oxidation by Pd supported on $CeO_2(100)$ and $CeO_2(111)$ facets, Appl. Catal., B 243 (2019) 36-46. https://doi.org/10.1016/j.apcatb.2018.10.015.

[43] G. Henkelman, H. Jónsson, Improved tangent estimate in the nudged elastic band method for finding minimum energy paths and saddle points, J. Chem. Phys. 113 (2000) 9978–9985, https://doi.org/10.1063/1.1323224.

[44] G. Henkelman, B.P. Uberuaga, H. Jónsson, A climbing image nudged elastic band method for finding saddle points and minimum energy paths, J. Chem. Phys. 113 (2000) 9901–9904, https://doi.org/10.1063/1.1329672.

[45] W Tang, E Sanville, G Henkelman, A grid-based Bader analysis algorithm without lattice bias, J. Phys.: Condens. Matter 21 (8) (2009) 084204, https://doi.org/10.1088/0953-8984/21/8/084204.

[46] P. Niton, A. Zywocinski, M. Fialkowski, R. Holyst, A "nano-windmill" driven by a flux of water vapour: a comparison to the rotating ATPase, Nanoscale 5 (2013) 9732–9738, https://doi.org/10.1039/C3NR03496H.

[47] I.A.W. Filot, R.A. van Santen, E.J.M. Hensen, The optimally performing Fischer-Tropsch catalyst, Angew. Chem., Int. Ed. 53 (2014) 12746-12750. https://doi.org/10.1002/anie.201406521.

[48] J. Deng, W. Song, M. Jing, T. Yu, Z. Zhao, C. Xu, J. Liu, A DFT and microkinetic study of HCHO catalytic oxidation mechanism over Pd/Co_3O_4 catalysts: The effect of metal-oxide interface, Catal. Today. 339 (2020) 210–219, https://doi.org/10.1016/j.cej.2018.08.195.

[49] Weiyu Song, Lulu Chen, Jianlin Deng, Meizan Jing, Huiling Zheng, Jian Liu, Zhen Zhao, Combination of density functional theory and microkinetic study to the Mn-doped CeO_2 catalysts for CO oxidation: A case study to understand the doping metal content, J. Phys. Chem. C 122 (44) (2018) 25290–25300, https://doi.org/10.1021/acs.jpcc.8b05885.

[50] X. Zhang, J. Liu, B. Zijlstra, I.A.W. Filot, Z. Zhou, S. Sun, E.J.M. Hensen, Optimum Cu nanoparticle catalysts for CO_2 hydrogenation towards methanol, Nano Energy 43 (2018) 200–209, https://doi.org/10.1016/j.nanoen.2017.11.021.

[51] Michael Nolan, Victor Soto Verdugo, Horia Metiu, Vacancy formation and CO adsorption on gold-doped ceria surfaces, Surf. Sci. 602 (16) (2008) 2734–2742, https://doi.org/10.1016/j.susc.2008.06.028.

[52] Ming-Wen Chang, Wen-Shyan Sheu, The charge states of Au on gold-substituted $Ce_{1-x}O_2(111)$ surfaces with multiple oxygen vacancies, Phys. Chem. Chem. Phys. 18 (23) (2016) 15884–15893, https://doi.org/10.1039/C6CP02647H.

[53] Ming-Wen Chang, Wen-Shyan Sheu, Water-gas-shift reaction on reduced gold-substituted $Ce_{1-x}O_2(111)$ surfaces: the role of Au charge, Phys. Chem. Chem. Phys. 19 (3) (2017) 2201–2206, https://doi.org/10.1039/C6CP07185F.

[54] V SHAPOVALOV, H METIU, Catalysis by doped oxides: CO oxidation by $Au_xCe_{1-x}O_2$, J. Catal. 245 (1) (2007) 205–214, https://doi.org/10.1016/j.jcat.2006.10.009.

[55] Eric W. McFarland, Horia Metiu, Catalysis by doped oxides, Chem. Rev. 113 (6) (2013) 4391–4427, https://doi.org/10.1021/cr300418s.

[56] Joachim Paier, Christopher Penschke, Joachim Sauer, Oxygen defects and surface chemistry of ceria: quantum chemical studies compared to experiment, Chem. Rev. 113 (6) (2013) 3949–3985, https://doi.org/10.1021/cr3004949.

[57] Michael Nolan, Stephen C. Parker, Graeme W. Watson, The electronic structure of oxygen vacancy defects at the low index surfaces of ceria, Surf. Sci. 595 (1-3) (2005) 223–232, https://doi.org/10.1016/j.susc.2005.08.015.

[58] T.X. Sayle, S.C. Parker, D.C. Sayle, Oxidising CO to CO_2 using ceria nanoparticles, Phys. Chem. Chem. Phys. 7 (2005) 2936–2941, https://doi.org/10.1039/B506359K.

[59] Donghai Mei, N. Aaron Deskins, Michel Dupuis, A density functional theory study of formaldehyde adsorption on ceria, Surf. Sci. 601 (21) (2007) 4993–5001, https://doi.org/10.1016/j.susc.2007.08.027.

[60] Bo-Tao Teng, Shi-Yu Jiang, Zong-Xian Yang, Meng-Fei Luo, You-Zhao Lan, A density functional theory study of formaldehyde adsorption and oxidation on $CeO_2(111)$ surface, Surf. Sci. 604 (1) (2010) 68–78, https://doi.org/10.1016/j.susc.2009.10.024.

[61] J. Deng, W. Song, L. Chen, L. Wang, M. Jing, Y. Ren, Z. Zhao, J. Liu, The effect of oxygen vacancies and water on HCHO catalytic oxidation over Co_3O_4 catalyst: A combination of density functional theory and microkinetic study, Chem. Eng. J. 355 (2019) 540–550, https://doi.org/10.1016/j.cej.2018.08.195.